Effect of Fe oxidation state (+2 versus +3) in precursor on the structure of Fe oxides/carbonates-based composites examined by XPS, FTIR and EXAFS

Natalia Chubar [a],[*], Vasyl Gerda [a],[b], Małgorzata Szlachta [a],[c], Ganna Yablokova [d]

[a] Department of Earth Sciences, Utrecht University, Budapestlaan 4, 3584 CD, Utrecht, Netherlands
[b] Faculty of Chemistry, Taras Shevchenko National University of Kyiv, Lva Tolstogo Street 12, 01601, Kyiv, Ukraine
[c] Geological Survey of Finland, P.O. Box 96, FI-02151, Espoo, Finland
[d] Department of Materials Engineering, KU Leuven, Kasteelpark Arenberg 44 Bus 2450, 3001, Leuven, Belgium

ABSTRACT

Here we investigate the influence of Fe oxidation state (either Fe(II) or Fe(III) sulfates) in precursor of the same chemical composition on the atomic scale structure, surface speciation and adsorptive anion removal of the purely inorganic composites produced under the urea supported hydrothermal synthesis. In case of utilization of Fe^{3+} precursor, the materials chemistry was solely dominated by the formation of highly crystalline Fe(III) oxides, however the particle surfaces were covered with small quantities of $FeCO_3$ (not detectable by EXAFS/XANES/FTIR) precipitated after the autoclave was turned off. Within the reactive medium with Fe^{2+} precursor, due to high pressure in autoclave which facilitated reducing conditions and sedimentation of Fe divalent, two main processes took place one of which was the formation of Fe hydrous oxides; the second reaction resulted in generation of $FeCO_3$, which become a predominant phase in volume averaged composition. Notably, despite the prevalence of Fe(II) carbonates in bulk structure, the narrow upper layers (XPS detectable) was enriched with Fe(III) oxides. At the chosen autoclave temperature of 150 °C, both samples had low hydration of physisorbed water, which confirmed our recent hypothesis about correlation between Fe (or another metal formed oxides) local structure in outer shells fitted with several (many) oxygen atoms and the material hydration with physisorbed water. None of the two composites demonstrated strong adsorptive removal of seven anions (F^-, Br^-, BrO_3^-, $HAsO_4^{2-}$, H_3AsO_3, HPO_4^{2-}, SeO_4^{2-}), which verified another idea about the interdependence of distinguished (EXAFS simulated) outer shells of metals (here, Fe) fitted with two paths simultaneously ({Fe–Fe}+{Fe–O}) one peak and the anion exchange potential. Overall, the Fe(III)-precursor product was more crystalline, less heterogeneous (fewer phases), showed worse anion uptake than the other sample. The material prepared from Fe(II) precursor is considered to be a promising precursor for further phase transformations via thermal or hydrothermal treatments (due to generous presence of $FeCO_3$).

1. Introduction

Iron oxides and carbonates are vital to society. They are useful in many geological and biological activities of the planet as well as played a prominent role in civilization evolution in general. Yet, despite an active exploration of iron oxides by humans since ancient time, their application in various industries has been extending nowadays. The list of fields of Fe oxides' utilization includes catalysis [1], water purification [2,3], energy storage [4], medicine, agriculture [5], cosmetics, pharmacy, biosensing, drug delivery and others [6,7]. New protecting and healing properties of iron oxides included in the composition of sunscreen products have been recently discovered [8]. Iron carbonates is one of the

popular green precursors for preparation of Fe oxides [9]; it can be used as food supplement for pets (cats and dogs) [10].

To date, 16 iron oxides have been reported including oxides, hydroxides and oxide-hydroxides. The well-known ones are goethite, akaganeite, lepidocrocite, magnetite, and hematite [11,12]. Although chemical composition of iron oxides is based on Fe, O and/or OH, their properties (and respectively) applications differ dramatically as a function of tiny variance in crystal regularities, iron oxidation state, speciation of each chemical element, hydration, degree of crystallinity, ratios between atoms and phases, and particularities of atomic scale structure in general. Researchers have been learning how to control these properties via establishing the correspondences between synthesis

conditions, structure and application.

Preparation method chosen to produce a particular material is a crucial step to design new materials with wanted performance. Hydrothermal precipitation of metal oxides ruled by hydrolysis of their various cations by urea transformations proved to be one of the popular approaches to develop the above solids for high technology applications such as catalysis, sorption, energy storage [13–15]. Slow decomposition of urea with increasing autoclave temperature provides favorable conditions for a step-wise formation of a variety of iron oxide/carbonate phases, which results in material heterogeneity and high surface reactivity.

After the synthetic method has been selected, experimental conditions and precursors must be chosen. Following the goal of obtaining iron oxides, wide variety of both raw materials (primarily, salts) and reagents (substances-hydrolyzers) have been explored by researchers to find regularities between the materials chemistry and the final solid properties. Predominant number of works are based on using one synthetic procedure for a particular application. Effects of precursors on the material structure were rarely explored in the past. For the reason that modern society requests new materials with predefined properties, nowadays more attention must be given to the studies, which establish regularities between fine details of the experimental conditions, first of all regarding precursors, and the material structure/properties/application.

Thus, Mishra et al. [16] investigated the influence of hydrolyzing agents on structural and magnetic properties of Fe_3O_4 produced from $FeCl_3 \cdot 6H_2O$. Liu et al. [17] discovered that iron salt anion (iron(III) nitrate and ammonium iron(III) citrate) had a significant influence on crystallinity, aggregation, composition of Fe–Co oxide nanoparticles in the continuous hydrothermal synthesis at the same cobalt salt precursor, which was helpful to deepen the knowledge on the reaction processes in order to better control the preparation of such composites. Cursaru et al. [18] synthesized magnetite nanoparticles from the same precursors but varying pressure and temperature, which affected the size and magnetization of the materials. Sayed et al. [19] reported six very different shapes of iron oxides synthesized using the same protocol (adding cetyltrimethlammonium bromide (CTAB) as a template, cyclohexane-water-pentanol as a reaction solvent and urea as hydrolyzing agent) but changing the iron salts as iron-precursors (Fe(II) sulfate, Fe(II) oxalate, Fe(III) chloride, Fe(III) nitrate, Fe(II) D-gluconate dehydrate, Fe(0) pentacarbonyl), which affected also the phase composition and magnetization. Typical syntheses are very often based on attracting organic templates or solvents. Okamoto et al. [20] revealed the effects of ligand and solvent on iron oxide nanoparticles obtained from iron(III) acetylacetonate solution by femtosecond laser irradiation. However, no reports were presented so far on the influence of Fe oxidation state (the only one variable – keeping the same salt anion) in purely inorganic synthesis under the urea-supported hydrothermal conditions from Fe inorganic salt.

In general, as concluded in the recent review [21], preparation of iron oxides is still a challenge, which requires more research to overcome the difficulties. One of the tasks is to better characterize such solids in order to obtain a deeper information on the entire material structure by attracting appropriate techniques, which allow characterization of both crystalline and amorphous phases. Majority of the works rely on using x-ray diffraction patterns (XRD), which characterizes crystalline phases only. This leaves an unknown part of usually complex material (which contains more than one phase including amorphous) uncharacterized.

In hydrothermal precipitation of Fe oxides, either Fe^{2+} or Fe^{3+} can be hydrolyzed, which will definitely result in different synthesis products. However, investigators are usually ground their reports on strictly defined singular preparation approach. Search for the best raw materials and investigation of the effects of precursor speciation (including oxidation state) are rare in articles.

Purely inorganic, urea supported hydrothermal precipitation,

reported in our previous works [22] proved to be a promising method for preparation of complex metals oxides for the adsorptive removal application. Nevertheless, the influence of Fe oxidation state in precursor on the composition and structure of the synthesis products has not been investigated yet.

The overall goal of this work was to study the differences in the material phase composition, atomic scale structure, surface chemistry and adsorptive anion removal as a function of Fe oxidation state in precursor: +3 versus +2, applying the same experimental conditions [22] including iron salt anion. It was achieved via performing the following tasks: using the previously well-tried experimental conditions (urea supported purely inorganic synthesis) to produce two Fe oxides/carbonates based composites from sulfates of Fe(II) and Fe(III): having only one variable – iron oxidation state; to compare the atomic scale structure of the entire composites (regardless of their crystallinity) by extended x-ray absorption fine structure (EXAFS) and x-ray absorption near edge structure (XANES); to investigate speciation of chemical elements on the surface of both Fe oxide/carbonate-based materials by x-ray photoelectron spectroscopy (XPS); to complement the above characterization techniques by Fourier-transform infra-red spectroscopy (FTIR) and x-ray diffraction (XRD); to test adsorptive removal of new composites of several anions (F^-, Br^-, BrO_3^-, $HAsO_4^{2-}$, H_3AsO_3, HPO_4^{2-}, SeO_4^{2-}); to verify the recently proposed methodological suggestions, which for the first-time correlated the EXAFS simulated extended fine structure around the main atoms in metal oxides (here, iron) in outer shells with the material properties: anion exchange via OH^- [2,3] and physisorbed water [14].

2. Materials and methods

2.1. Synthesis of composites based on Fe oxides/carbonates

The same experimental conditions as those used in the previous work [14] were applied to the material preparation. Their important features/principles were: purely inorganic synthesis (no organic solvents and reagents); reasonably high temperature (not too high, energy saving); sufficient but not too long contact time (energy/labor effective); using urea as hydrolyzing agent (alkalis avoided). Urea was especially chosen to run hydrolysis of Fe cations due to its slow decomposition, which causes a step-wise formation of various phases of Fe precipitates in autoclave that provides heterogeneity to the material and increases a number of sorption sites. The latter results in high surface reactivity making the material a better adsorbent or catalyst.

Divalent and trivalent salts of Fe ($FeSO_4$ and $Fe_2(SO_4)_3$) were used as precursors in one-stage synthesis. Calculated quantities of solid substances of iron sulfates, urea (Sigma–Aldrich chemicals of analytical grade) as well as deionized water were added into 1 L autoclave in the ratio: 0.06, 0.16 and 40.0 mol, respectively. The mixture was stirred, the autoclave was sealed and moved into oven for 24 h at the temperature fixed at 150 °C after which the autoclave was turned off and left to cool at ambient temperature till the next day. Generated solids were filtered on membrane filter of 0.25 μm diameter, washed with generous amounts of ultra-pure water and rinsed with ethanol. The formed composites were dried in air-flow oven at 80 °C.

The products resulted from the above synthesis were the powders of brown color. During the research period, there was no changes in the particle appearance in both samples, over several months.

For convenience, in this work the samples will be further referred as "Fe(II)-150" and "Fe(III)-150" according to Fe-containing precursor (sulfate of either Fe(II) or Fe(II)) at the autoclave temperature of 150 °C.

2.2. X-ray absorption near edge structure (XANES), extended x-ray absorption fine structure (EXAFS) and simulation of the latter

Fe K-edge (7112 eV) spectra were collected at the Dutch-Belgian (DUBBLE) beamline (BM26A) of the European Synchrotron Radiation

Facilities (ESRF), Grenoble, France. The beamline was equipped with a Si(111) double-crystal monochromator. All measurements were carried out in the transmission detection mode at ambient temperature. A contemporary experimental setup of the DUBBLE beamline was presented in Ref. [23]. IFFEFIT software package composed of Athena, Artemis, and Atoms was used to process and simulate EXAFS data [24]. The linear combination fitting (LCF) option of the Athena software allowed estimation of the main compounds in the samples as well as their percentages and ratios. LCF was grounded on combinations of XANES spectra of the reference materials written at the same beamline (DUBBLE): Fe_2O_3, FeOOH, FeO, Fe_3O_4, $FeCO_3$, Fe(II)/Fe(III) oxide. The local structure around Fe was simulated using the input files (feff.inp) generated from the crystallographic data of several compounds: α-Fe_2O_3 (hematite), β-iron oxide, siderite ($FeCO_3$), FeO, akaganeite [25] and magnetite (Fe_3O_4) [26]. To make a choice of the right path (obtained from feff.inp files) for the fitting we reviewed distances of various paths by plotting them together with the experimental spectra in order to select the closest one for the final fits. We distinguished the backscattering oscillations from heavy and light atoms by changing k-weighting of the spectra as well as empirically. For the latter, Artemis software differentiates backscattering from heavy (Fe–Fe) and light (Fe–O) chemical elements to Fe-absorber. For instance, we would not be able to achieve fitting if we have tried to simulate Fe–Fe feature by Fe–O path. The Fourier-transforms (FT) peaks were modeled stepwise, starting from the first shell. To fit the next shell, we included an additional (carefully chosen) path in the model.

2.3. Fourier transform infrared (FTIR), x-ray photoelectron spectroscopy (XPS) and x-ray diffraction patterns (XRD)

FTIR spectra were recorded on a Nicolet 6700 Fourier transform infrared spectrometer within the range of 400–4000 cm^{-1} with 32 scans at a resolution of 2 cm^{-1} using the conventional KBr pellet method in transmission mode. KBr pellets were formulated on Specac manual hydraulic press at no more than 10 T pressure (typically, 8–9 T).

Surface analysis by XPS was carried out on a Kratos Axis Ultra DLD electron spectrometer utilizing monochromated Al Kα source operated at 150 W. The spectrometer neutralization system was used to stabilize the surface potential. Wide-spectrum (survey) was written at the pass energy of 160 eV; high-resolution spectra of all detected elements were acquired at 20 eV. The binding energy (BE) scale was referenced to the C 1s peak of aliphatic carbon which was set at 285.0 eV. The analysis area was 0.3–0.7 mm^2, and the depth of measurements ~5–6 nm. Base pressure in chamber constituted $1 \cdot 10^{-7}$ Pa. Spectral processing (Shirly background subtraction and fitting with Gauss/Lorentz peak components) was done using software Vision2 Kratos.

XRD patterns were collected on a Bruker-AXS D8 Advance powder X-ray diffractometer equipped with an automatic divergence slit, Vantec-1 detector, and Co$K\alpha$1,2 ($\lambda = 1.79026$ A) source.

2.4. Evaluation of samples Fe(II)-150 and Fe(III)-150 for their anion removal capability: brief adsorption experiments

The best approach to estimate the potential of a new material as a future sorbents/anion exchanger is to run preliminary batch adsorption tests under the experimental conditions, which allow to measure an approximate removal capacity of the material at saturation of adsorptive sites. Since the samples based on metal oxides are classical anion exchangers (due to an occurrence of the surface OH^- groups, capable for anion exchange with aqueous anionic species) we tested an ability of Fe (II)-150 and Fe(III)-150 to remove anions from water solutions. However, adsorptive affinity of the two participants of the interfacial processes is a function of two variables, adsorbent and adsorbate, as well as their properties. Promising removal (or negligible uptake) of one aqueous anion by the material does not guarantee a competitive sorption of another (adsorbate) anion. Therefore, a long list of the anions

(F^-, Br^-, BrO_3^-, $HAsO_4^{2-}$, H_3AsO_3, HPO_4^{2-}, SeO_4^{2-}) were involved in the experiments, which tested an adsorptive capability of the experimental samples.

One-point batch sorption tests were run at ambient temperature (20 $\pm$ 2 °C) and pH = 6.7 $\pm$ 0.2 adjusted with 0.1 N HNO_3 and NaOH. The initial concentration of each anion (F^-, Br^- and BrO_3^-, $H_2AsO_4^-$, As(III), $H_2PO_4^-$, SeO_4^{2-}) was set at 200 $\pm$ 15 mg/L measured by chemical element for complex anions, such as mg[As]/L for arsenate or arsenite. The literature revealed that such level of the aqueous anion content is high enough to saturate sorption sites of the most competitive inorganic anion exchangers. This enabled us to estimate an approximate adsorptive capacities of Fe(II)-150 and Fe(III)-150.

We set the solid/liquid ratio (an adsorbent dose) at 2 g/L, which provided the information on the reliable anion uptake performance of the samples. It has been noted that within an adsorbent dose of 2–5 g/L, the removal capability of the most promising adsorbents does not depend on the solid/liquid ratio, as reflected by the plateau on the respective curves.

Batch adsorption experiments were carried out in 50 ml polyethylene tubes. Accurately, 40 ($\pm$3) mg of adsorbent was added to 20 ml of anion aqueous solution in background electrolyte 0.1 N $NaNO_3$. The batches were kept on shaker at 200 rpm until equilibrium after which the solution was separated from the material by filtration, in which the remaining concentrations of anion was measured. The uptake of anions by the composites was determined using the standard empirical formula (1):

$$q = \frac{(C_o - C_{eq.})V}{m},\qquad(1)$$

where q (mg/g) is the amount of anion sorbed per gram of the adsorbent (dry weight), C_o (mg/L) is the initial concentration of the anion (as P, As, Br), C_{eq} (mg/L) is the final (or equilibrium) concentration of the anion in solution, V (mL) is the volume of the solution, and m (mg) is the weight of adsorbent.

Concentrations of P, As, Fe, Se in aqueous adsorbate were quantified by inductively coupled plasma optical emission spectrometry (ICP-OES); F^-, Br^- and BrO_3^- were measured using ion chromatography.

3. Results

3.1. Fourier transform infrared spectra (FTIR) in samples Fe(II)-150 and Fe(III)-150

FTIR spectra in Fe(II)-150 and Fe(III)-150 are presented in Fig. 1 and S1 (S - Supplementary supporting information). The latter shows the full range of IR-irradiation wavenumbers applied, at 400-4000 cm^{-1}. Even a quick glance at the FTIR spectra (Fig. 1) points out on sharp difference in the composition of two samples. It is obvious that Fe(II)-150 was predominantly composed of Fe carbonates the presence of which was expressively manifested by the characteristic bands at 1416, 862 and 739 cm^{-1}. Any small admixtures of metal carbonates under the IR-irradiation always produce the thin high peaks at 862 and 739 cm^{-1}, which are not overlapped with vibrations of other bonds, and consequently cannot be confused with reflections of another compound. Phases of Fe oxides in sample Fe(II)-150 were recognized in FTIR spectrum from an occurrence of the two peaks (at 567 and 463 cm^{-1}) in the IR region of vibrations of Fe–O (metal-O) and Fe–O–Fe. Even though the IR features of Fe–O bands were smaller compared with the peaks resulted from vibrations of CO_3^{2-}, an existence of iron oxide-based phases were confirmed by FTIR also in Fe(II)-150.

In contrast to Fe(II)-150 dominated by Fe carbonates, FTIR investigation of Fe(III)-150 did not identify a presence of iron carbonates in any quantities detectable by IR-spectroscopy in the entire bulk of the material. It is known that FTIR spectroscopy can reveals >1–5% of phase admixtures in complex minerals. Looking ahead, XPS surface analysis
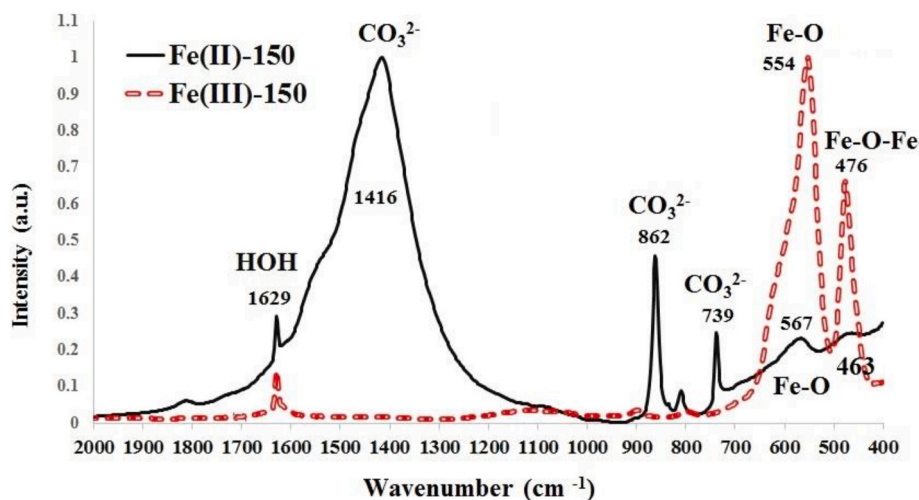
Fig. 1. FTIR spectra in Fe(II)-150 (unbroken black line) and Fe(III)-150 (dotted red line). (For interpretation of the references to color in this figure legend, the reader is referred to the Web version of this article.)

(which measures only very thin layer of a solid surface) defined the presence of 1.35 at.% of C as carbonate species in the upper 50 Å layer of Fe(III)-150 surface. After this small quantity of the surface $FeCO_3$ was volume averaged, its concentration in the entire sample became much smaller than 1%, detectable by FTIR technique. Not surprising that FTIR did not discover any siderite ($FeCO_3$) in Fe(III)-150, which is solely composed of Fe oxide phases reflected by very high sharp bands at 476 and 554 cm^{-1}, as obvious from Fig. 1. Such two bands in the same ratio at approximately 440–460 and 530 are characteristic of hematite [27], however hematite-assigned peaks can be found also at a broader range in the same IR-region, depending on a sample composition and complexity. The feature at 554 cm^{-1} was assigned to Fe–O stretching modes, while at the other one at 475 cm^{-1} was attributed to bending vibrations of Fe–O–Fe.

Bands at 1639 cm^{-1} were generated due to the vibrations of physisorbed water in the material structure. Small size of these peaks in both samples indicated that Fe(II)-150 and Fe(III)-150 were pretty dry materials with tiny quantities of physisorbed water. For comparison, the sample based on Fe oxides/carbonates named Fe-180 in Ref. [14] had an approximately twenty times more physisorbed water (reflected by the respective peak at 1639 cm^{-1}) than any of the composites, Fe(II)-150 or Fe(III)-150.

3.2. X-ray data in Fe(III)-150 from XRD patterns

Fig. 2 and Table 1 present results of Fe(III)-150 examination by XRD. Incidentally, no XRD patterns was collected for sample Fe(II)-150, however it was defined in our previous work [14] that the three composites based on Fe oxides/carbonates produced from Fe(II) divalent precursor at the autoclave temperatures of 120, 150 and 180 °C were composed of the same three crystalline phases: maghemite, γ-Fe_2O_3 (Ref. Code 00-25-1402), magnetite, Fe_3O_4 (Ref. Code 01-082-1533) and siderite, $FeCO_3$ (Ref. Code 01-083-1764).

Based on XRD patterns, the samples synthesized from Fe(II) salt were dominated by (or always contained) Fe carbonates, siderite [14]. In contrast, siderite was not detected by XRD in Fe(III)-150, the sample produced from Fe(III) trivalent salt. Two Fe-containing crystalline phases were revealed: hematite (α-Fe_2O_3) (Ref. Code 01-079-1741) and hydrohematite ($Fe_{1.833}(OH)_{0.5}O_{2.5}$) (Ref. Code 01-076-0182), see Fig. 1 and Table 1. This outcome correlates with the XANES LCF simulation. Excellent quality of the linear combination fitting for Fe(III)-150 was based on using only two different Fe(III) oxides while introduction of other compounds, such as carbonates or hydroxides, always worsen the quality of LCF modeling.
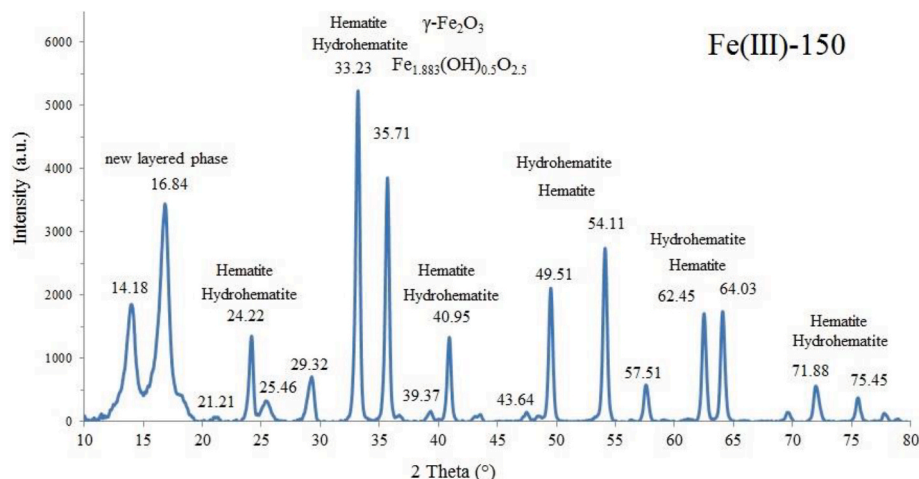

Fig. 2. XRD patterns in Fe(III)-150.

Table 1
X-ray data from XRD patterns in sample Fe(III)-150.

2Θ (deg)	d (Å)	I/I₀
14.184	6.244	25.3
16.840	5.265	63.5
18.409	4.820	5.2
21.206	4.190	1.3
24.215	3.676	25.8
25.460	3.499	6.3
29.321	3.046	13.1
31.775	2.816	0.4
33.230	2.696	100.0
35.710	2.514	74.9
36.804	2.442	1.6
39.368	2.289	3.2
40.954	2.204	25.9
43.269	2.089	0.3
43.642	2.074	1.8
47.514	1.914	2.7
48.541	1.874	0.2
49.506	1.841	41.1
54.114	1.695	53.4
56.298	1.634	0.6
57.508	1.603	10.6
58.967	1.566	0.5
60.901	1.521	0.6
62.445	1.487	31.9
64.026	1.454	32.9
65.935	1.417	0.3
69.603	1.351	2.9
71.883	1.313	10.2
75.448	1.260	6.7
77.737	1.229	2.6
78.837	1.214	0.8
80.835	1.189	4.5
82.853	1.165	4.1
84.894	1.142	7.1
88.513	1.105	7.0
91.412	1.077	0.7
93.622	1.057	6.9
95.640	1.039	2.3

3.3. XANES analysis in two experimental samples, Fe(II)-150 and Fe(III)-150

Fig. 3 presents XANES spectra in Fe(II)-150 and Fe(III)-150 together with the relevant reference materials of divalent Fe (FeO) and trivalent (Fe_2O_3 and FeOOH). Plotting the spectra of the above-mentioned
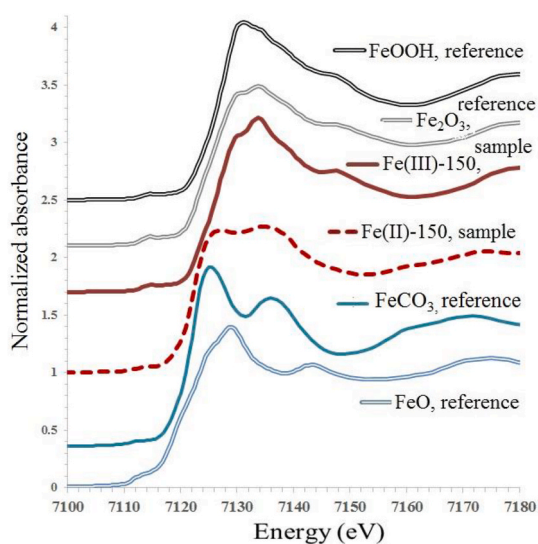

Fig. 3. XANES spectra in samples Fe(II)-150 and Fe(III)-150 as well as in the references: FeO, Fe_2O_3 and FeOOH.

standards helped directly anticipate the dominating oxidation state of Fe in each sample, which was obvious based on the first inflection points on the graphs.

We can anticipate from Fig. 3 that predominant oxidation state of Fe in Fe(II)-150 is Fe^{2+}, however the iron compound species were different from iron oxides, which was clear from the shapes of XANES in the sample and the reference FeO. On the other hand, its resemblance with XANES of the reference $FeCO_3$ is obvious, even if the latter is not the only phase in this material. Comparison of the XANES data in composite Fe(III)-150 and the reference Fe_2O_3 strictly pointed out on their similarity, which encouraged a preliminary conclusion about Fe(III) oxides as the main phase in Fe(III)-150. This prediction was confirmed by the LCF (see Table 2), which demonstrated that the main compound in Fe(II)-150 was $FeCO_3$ (56.2%) whereas two different species of Fe oxides constituted Fe(III)-150 with excellent quality of the LCF fitting, see Fig. S2 (Supplementary supporting information).

The pre-edge and near-edge regions of XANES (see Fig. S3) were reviewed in order to evaluate the ratio between Fe^{2+} and Fe^{3+} in samples Fe(II)-150 and Fe(III)-150 (see Fig. S4). Based on the numerical data in the near-edge region of XANES spectra, it was calculated that (the entire sample) Fe(III)-150 was 100% composed of Fe(III) substances. In composite Fe(II)-150, the ratio of Fe^{2+}/Fe^{3+} constituted 68/32%, respectively. Tiny quantities of Fe(II) carbonate on the surface of Fe(III)-150 (after being volume averaged) were not discovered by this method. Taking into account the detection limit of XANES, the correlation between the LCF (Table 2) and the results of examination of the XANES pre-edge region (Fig. S3) was very satisfactory.

3.4. EXAFS spectra and their simulation in Fe(II)-150 and Fe(III)-150

Fe K-edge EXAFS in Fe(II)-150 (A) and Fe(III)-150 (B) are reflected in Fig. S5 together with the respective fits. Fig. 4 presents the radial structure around Fe resulted from Fourier transforms of Fe K-edge EXAFS oscillations in the same samples as well as some data from EXAFS simulation pointing on the atoms (Fe, O or C) backscattering from a particular distance to Fe-absorber. The outcome of EXAFS simulations is gathered in Table 3, which is accompanied by table S1 (the latter reports the list of the paths obtained from crystallographic information of various minerals used in modeling).

Doublet in the first shell of Fe(II)-150 was fitted with three oxygen (O) atoms each feature at 2.01 and 2.12 Å using Fe–O paths generated from crystallographic information of akageneite, see Table 3 and Fig. 4. Interestingly, that Fe–O distance in the first doublet peak (2.01 Å) by value approached the second peak distance in the reference mineral akageneite (2.04 Å) (see table S1). The interval from Fe-absorber to the second doublet peak (2.12 Å) was close to the first shell length in siderite (2.15 Å). At the same time, Fe(II)-150 preserved the regularities of akageneite in Fe first shell keeping distances between two peaks of doublet at 10–12 Å (2.12–2.02 Å in sample Fe(II)-150; 2.04–1.92 Å in mineral akageneite).

Table 2
Results of the LCF based on XANES spectra in composites Fe(II)-150 and Fe(III)-150, % of the reference compound, and the ratios of Fe^{2+}/Fe^{3+} estimated from the near-edge region of XANES spectra.

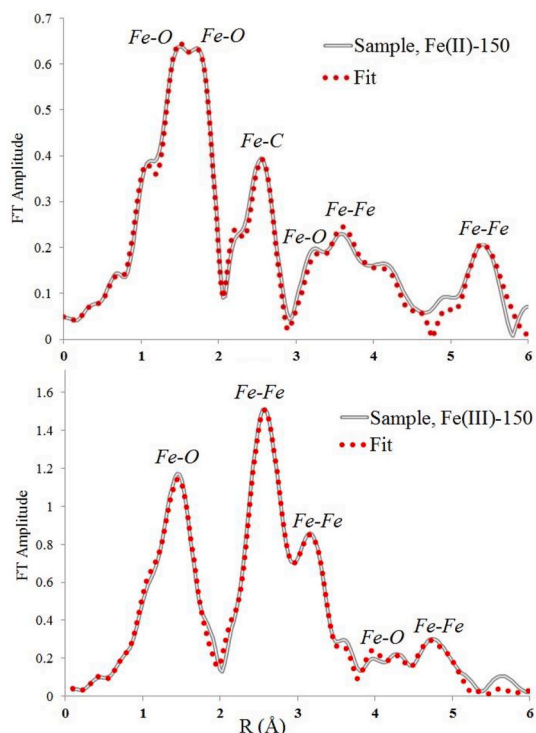| Reference	Sample	
	Fe(II)-150	Fe(III)-150
Fe_2O_3	43.8%	26%
Fe(III) oxide	-	74%
FeOOH	-	-
FeO	-	-
$FeCO_3$	56.2%	-
Fe(II)Fe(III) oxide	-	-
Ratio Fe^{2+}/Fe^{3+} from near-edge	68% Fe^{2+} 32% Fe^{3+}	100% Fe^{3+}

Fig. 4. Radial structure around Fe resulted from Fourier transforms of Fe K-edge EXAFS oscillations in samples Fe(II)-120 and Fe(III)-150.

Table 3

Cluster structure data resulted from Fe K-edge EXAFS simulation and crystallographic information used in the fitting. R—interatomic distance, CN—coordination number, σ^2—the Debye–Waller mean square disorder factor, ΔE_0—energy shift parameter, R-factor—goodness of the fit.

Sample	Path	R, Å	CN	σ^2 (Å^2)	ΔE_0 (eV)	R-factor
Fe(II)-150	Fe–O (Akaganeite)	2.01	3.0	0.0026	10.00	0.0250
	Fe–O (Akaganeite)	2.12	3.0	0.0028	−7.08	
	Fe–C (Siderite)	3.03	10.0	0.0046	7.50	
	Fe–O (Akaganeite)	3.70	2.0	0.0033	−10.00	
	Fe–Fe (Magnetite)	4.04	2.0	0.0230	−7.95	
	Fe–Fe (Akaganeite)	5.81	4.0	0.0065	6.60	
Fe(III)-150	Fe–O (Fe$_2$O$_3$, β-iron oxide)	1.95	6	0.0106	−8.406	0.0090
	Fe–Fe (β-iron oxide)	3.00	6	0.0081	3.473	
	Fe–Fe (Siderite)	3.66	2	0.0027	−6.961	
	Fe–O (Hematite)	4.74	3	0.0042	10.000	
	Fe–Fe (Hematite)	5.16	8	0.0129	9.998	

Note: See the paths which were used for the fits in table S1 (Supplementary materials).

The biggest peak of Fe second shell in Fe(II)-150 was fitted with 10 carbon (C) atoms at 3.03 Å using the main Fe–C path from siderite (with crystallographic distance of 2.99 Å). Remarkably, Fe–C distances in Fe(II)-150 (calculated) and in siderite (reference mineral) are very close, which proved the fact of the predominant occurrence of Fe carbonates in this composite. The other EXAFS feature in the second shell was modeled with 2 O atoms at 3.7 Å.

The first shell of Fe in Fe(III)-150 (single peak) was simulated with 6 O atoms at 1.95 Å applying Fe–O path obtained from crystallographic data of Fe$_2$O$_3$ (β-Fe oxide). The above distance was nearly the same as the Fe–O interval of the first doublet peak in hematite, the first shell of which was modeled with two Fe–O paths based on feff.inp file. Despite the fact that Fe(III)-150 was greatly composed by two highly crystalline phases, hematite and hydrohematite, both of the 1st shell doublet paths

obtained from hematite crystallographic information (two Fe–O distances at 1.95 and 2.12 Å) were not applicable to EXAFS simulation strategy of Fe local structure in this sample. The second shell of Fe in Fe(III)-150 was very characteristic of highly crystalline metal oxides whose second shells (formed due to the oscillations from heavy atoms, and respectively, fitted with Fe–Fe paths) were bigger than the first shells (resulted from backscattering of lighter atom, O, and correspondingly, modeled with Fe–O paths). The first band in Fe second shell region was simulated with 6 Fe atoms at 3.00 Å; the second peak was fitted with 2 Fe atoms at 3.66 Å.

Outer shells of Fe in Fe(II)-150 were simulated with two Fe–Fe distances, one of which was fitted with two Fe atoms at 4.04 Å and the second was modeled with four Fe atoms at 5.81 Å. Quality of the fits was never improved if oxygen was included in the simulation strategy of Fe environment in this sample. Local structure around Fe in outer shell in Fe(III)-150 was modeled using Fe–O and Fe–Fe paths, each of which fitted different peak. The shorter distance was simulated with three O atoms at 4.74 Å; the longer one was fitted with 8 Fe atoms at 5.16 Å. Notably: in none of the samples, Fe(II)-150 and Fe(III)-150, not a single peak in the outer shell was modeled using simultaneously two different paths, {Fe–Fe}+{Fe–O}, to fit the same band.

In order to better imagine the structure of metal oxide-based composites we visualized the results of EXAFS simulation in a graph, which displayed each shell of Fe local structure separately (Fig. 5) We plotted also the respective paths of feff.inp files, which were either utilized in simulation of a particular shell or were useful in discussion. Such results are easier to interpret (imagine) than standard presentation of numbers in tables. Fig. 5 shows the outcome of EXAFS simulation in Fe(II)-120 and Fe(III)-150 grouped by shells: A – first shell, B – second shell and C – further shells. The first shell of Fe in Fe(II)-150 (Fig. 5) looked similar to the 1st shell regularity in akageneite (also two doublet bands), however Fe–O distances in the doublet first and second peaks were very close to those in Fe β-oxide (2.01 Å in both materials) and siderite (2.12 Å in sample versus 2.15 Å in siderite), respectively, see Fig. 5, Table 3 and S1.

The 1st (singular peak) shell distance of Fe–O in Fe(III)-150 matched to the first doublet peak in hematite; in both materials it constituted 1.95 Å.

Simulation of the second Fe shells in both experimental samples correlated with the XANES LCF (Table 2) as well as with the 1st shell information. Although the strongest second shell peak in Fe(II)-150 was fitted with the closest (major) Fe–C distance of siderite, indicating a domination of iron carbonate in this sample, the entire Fe 2nd shell of which diffed from that in siderite whose second shell must be modeled with two Fe–C distances (see Fig. 5). Instead, the presence of Fe oxide phases in Fe(II)-150 was shown by Fe–O distance in the second shell. The Fe second shell in Fe(III)-150 was solely simulated with Fe–Fe paths (a characteristic second shell in metal oxides), which reaffirmed that this material was composed of several phases of Fe oxides.

Unlike in many nanomaterials, the Fe outer shells were clearly visible in both, Fe(II)-150 and Fe(III)-150, however in the former it was more expressive then in the latter. None of the peaks in any of the samples in this region was refined using simultaneously two paths: {Fe–Fe}+{Fe–O}, which, due to our previous methodological suggestion [2,3], indicated a poorly developed surface chemistry of a potential future anion exchanger appeared as surface OH$^-$ groups to be exchanged with aqueous anions. We observed in the previous papers [2,3] that indeed such materials (characterized by the outer shell of the main atom regularities described above) were not the strong anion removers, which was validated in Ref. [14].

3.5. Characterization of surface chemistry in Fe(II)-150 and Fe(III)-150 by X-ray photoelectron spectroscopy (XPS)

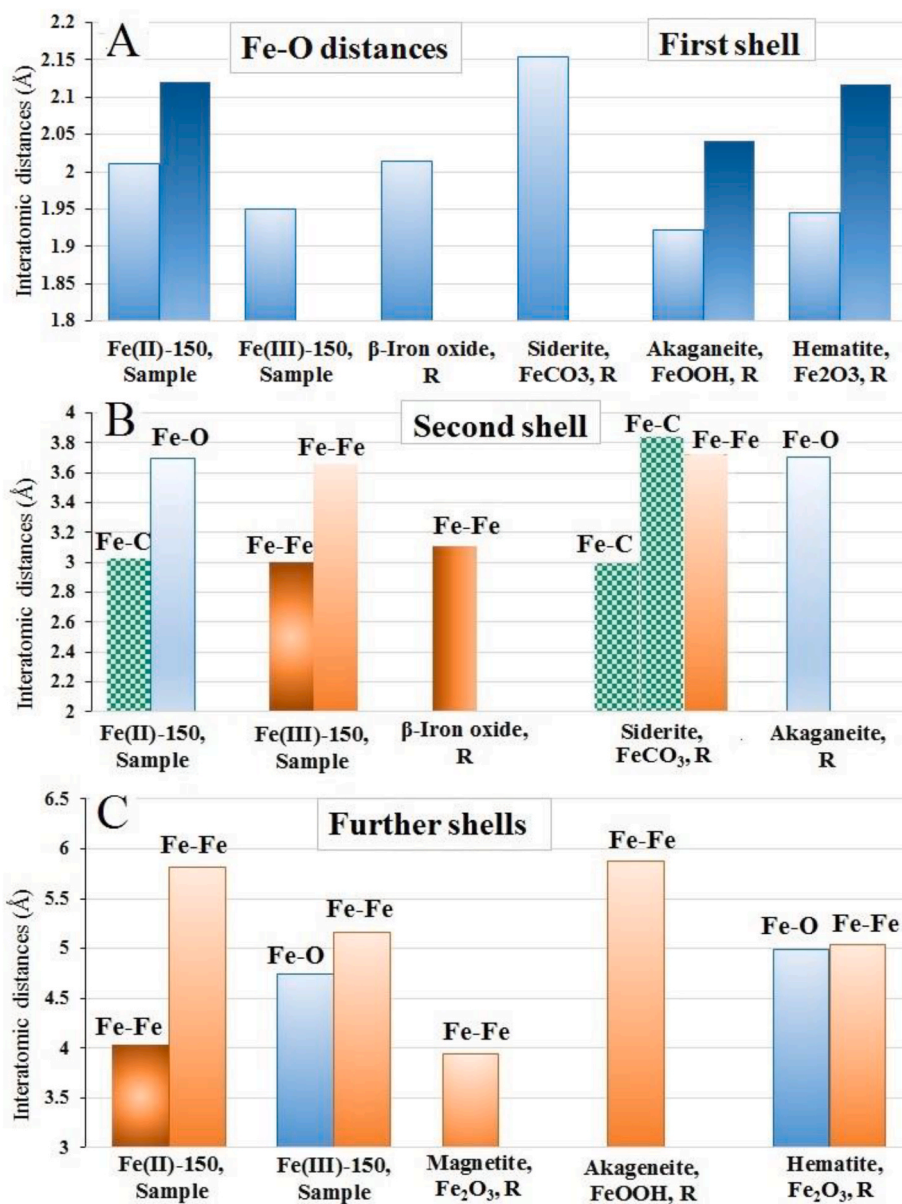Results of XPS analysis in Fe(II)-150 and Fe(III)-150 are presented in Tables 4 and 5 and Figs. 6–8.

Fig. 5. Graphical display of the interatomic distances between Fe-absorber and backscattering atoms (Fe, O and C) in Fe(II)-150 and Fe(III)-150 based on Table 2, and some paths from the reference materials used in the final fits. Note: "R" means reference.

Table 4
XPS features in Fe-oxides/carbonates-based composites produced from Fe(II) and Fe(III)-valent precursors at 150 °C autoclave temperature in samples Fe(II)-150 and Fe(III)-150, respectively.

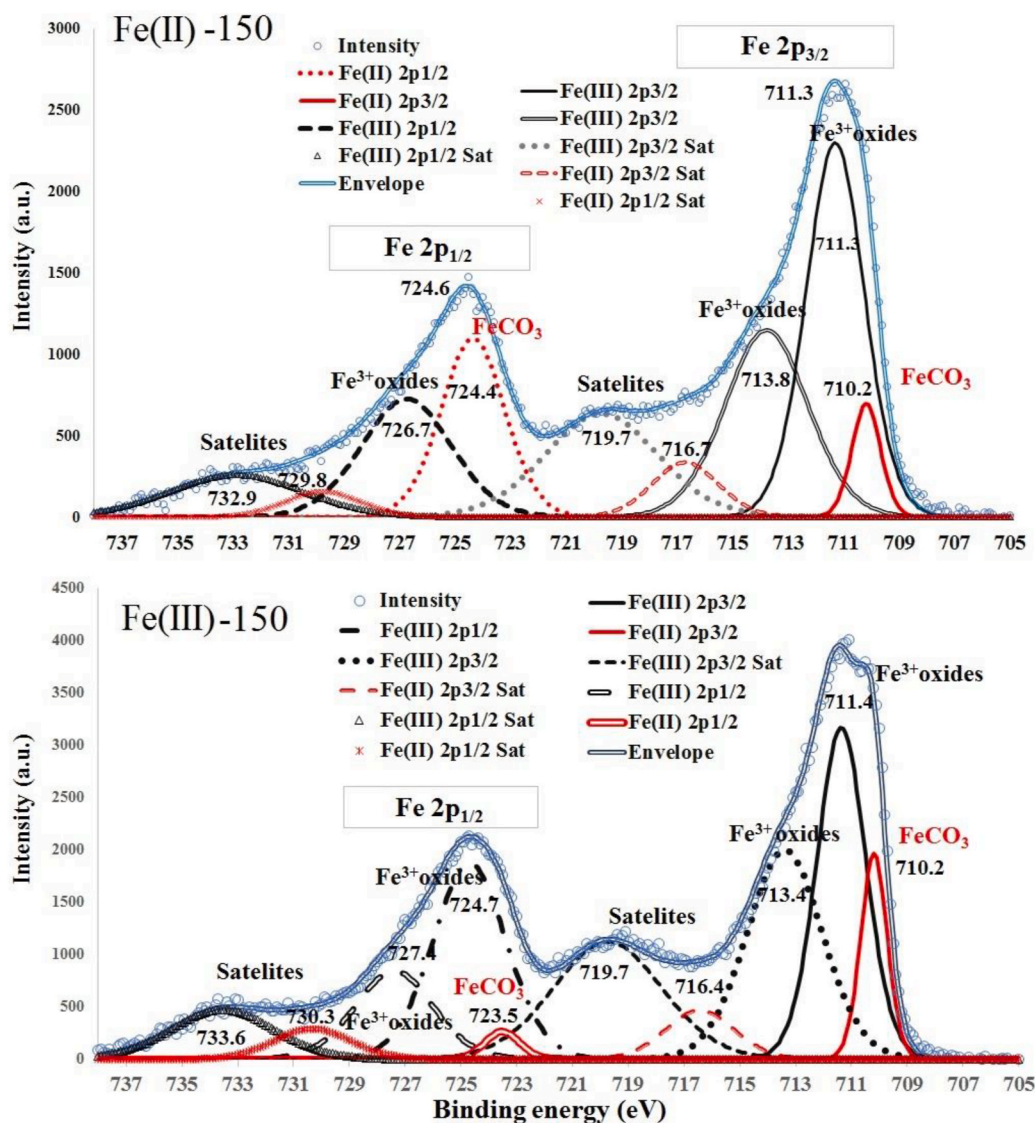|	Sample Fe(II)-150			Sample Fe(III)-150			
Line	BE, eV	FWHM, eV	AC, at.%	BE, eV	FWHM, eV	AC, at.%	Assignment
Total Fe 2p			29.27			34.14	See Table 5
	Oxygen (O) XPS features						
O 1s	530.4	1.25	23.81	530.4	1.01	41.67	O^{2-} (Fe–O)
O 1s	532.3	1.50	29.89	531.8	1.17	9.06	CO_3^{2-}, OH^- ($FeCO_3$)
O 1s	–	–	–	532.8	1.58	2.43	(H_2O)
	Carbon (C) XPS features						
C 1s	285.0	1.35	3.49	285.0	1.21	8.02	C–H (contamination, organic)
C 1s	286.2	1.30	1.26	286.2	1.82	3.33	C–O (contamination, org.)
C 1s	288.7	1.03	1.16	–	–	–	HCO_3^-
C 1s	290.2	1.105	9.28	289.0	1.36	1.35	CO_3^{2-}

Fig. 6 shows Fe 2p XPS spectra in Fe(II)-150 (upper graph) and Fe (III)-150 (lower plot); it is accompanied by Table 5 which systematized the available XPS features (binding energies and their assignments)

of Fe 2p spectra deconvoluted. It is known that in solid materials XPS peak positions of atoms are strongly dependent on its environment. Binding energies of metals in individual compound phase (such as metal

Table 5

Binding energies of Fe 2p XPS features in samples Fe(II)-150 and Fe(III)-150, associated with Fig. 6. "Sat" – satellite.

Sample	Binding energy (eV)									
Line	Fe2p$_{3/2}$	Fe2p$_{3/2}$	Fe2p$_{3/2}$	Sat.1	Sat.2	Fe2p$_{1/2}$	Fe2p$_{1/2}$	Fe2p$_{1/2}$	Sat.3	Sat.4
Fe(II)-150	710.2	711.3	713.8	716.7	719.7	724.4	–	726.7	729.8	732.9
Fe(III)-150	710.2	711.4	713.4	716.4	719.7	723.5	724.7	727.4	730.3	733.6
Interpret.	Fe^{2+}, FeCO$_3$	Fe^{3+} oxides	Fe^{3+} oxides, different species	Sat. Fe(II) 2p$_{3/2}$	Sat. Fe(III) 2p$_{3/2}$	Fe^{2+}, FeCO$_3$	Fe^{3+} oxides	Fe^{3+} oxides, different species	Sat. Fe(II) 2p$_{1/2}$	Sat. Fe(III) 2p$_{1/2}$

Fig. 6. Fe 2p XPS spectra in samples in Fe(II)-150 (upper graph) and Fe(III)-150 (lower plot).

oxide) would be shifted if this same phase would become a part of inorganic composite (surrounded by different phases). Thus, interpretation of XPS analysis in complex materials requires careful consideration as well as taking into account finding of other researchers shared in their publications. In individual substances FeO and Fe$_2$O$_3$, BEs of Fe 2p$_{3/2}$ were reported at 709.6 and 710.8 eV, respectively [28]; however, in Ni–Fe bimetallic catalysts, BE of Fe(III) 2p$_{3/2}$ was measured at 712.8–713.4 eV [29]. Fe XPS 2p profile in Fe oxides, featured at 709.1, 710.6 and 713.4 eV, was interpreted as Fe^{2+}$_{octahedral}$ (in FeO), Fe$^{3+octahedral}$ and Fe^{3+}$_{tetrahedral}$, respectively [30]. Grosvenor [31] reported the main peaks of Fe^{2+} 2p$_{3/2}$ in FeO (wustite), FeCl$_2$ and FeSO$_4$ at

709.5, 710.6 and 711.0 eV, respectively. Matamoros-Veloza et al. [32] measured the first peaks of Fe 2p$_{3/2}$ in FeCO$_3$ at 709.8 and 710.3 at different experimental conditions (pH values). In Ref. [33], which examined transformations of siderite into goethite by humic acids in the presence of H$_2$O$_2$ in natural environment, BEs of XPS peaks of Fe 2p$_{3/2}$ and Fe 2p$_{1/2}$ were measured at 709.1–710.2 eV and 722.5–724.5 eV, respectively, as a function of humic acid precipitation; an appearance of peak at 712.3 eV was a consequence of Fe(II) oxidation in FeCO$_3$ (siderite) and the formation of Fe(III) oxides.

Deconvolution of XPS Fe 2p$_{3/2}$ profile in composite Fe(II)-150 revealed three Fe species at 710.2, 711.3 and 713.8 eV; in sample Fe
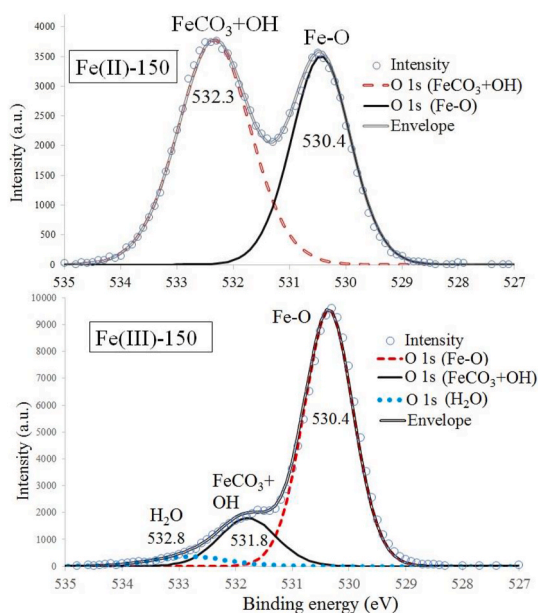
Fig. 7. O 1s XPS spectra in Fe(II)-150 (upper) and Fe(III)-150 (lower).

(III)-150 at 710.2, 711.4 and 713.4 eV the first of which (at 710.2 eV) was assigned to Fe^{2+} in $FeCO_3$, while the other two were attributed to Fe^{3+} hydrous oxides, respectively. Satellites of Fe^{2+} $2p_{3/2}$ were found at 716.7 and 716.4 eV in Fe(II)-150 and Fe(III)-150, respectively. Fe^{3+} $2p_{3/2}$ satellites were measured at 719.7 eV in both samples. Fe $2p_{1/2}$ profiles in Fe(II)-150 was deconvoluted into two peaks, at 724.4 and 726.7 eV, to be assigned to Fe^{2+} $2p_{1/2}$ and Fe^{3+} $2p_{1/2}$, respectively. In Fe(III)-150, it was decomposed into three peaks, at 723.5, 724.7 eV, 727.4 eV, respectively, attributed to Fe^{2+} $2p_{1/2}$ (first band) and Fe^{3+} $2p_{1/2}$ (the other two features), sequentially. Satellites in Fe $2p_{1/2}$ profile were measured at 729.8/730.3 eV and 732.9/733.6 eV for Fe^{2+} $2p_{1/2}$ and Fe^{3+} $2p_{1/2}$, in samples Fe(II)-150/Fe(III)-150, respectively.

Fig. 7 presents the speciation of surface oxygen from O 1s XPS spectra in Fe(II)-150 (upper graph) and Fe(III)-150 (lower plot). Slight predominance of Fe carbonates over Fe oxides on the surface of Fe(II)-150 was verified. O 1s XPS feature at 532.4 eV assigned to carbonate [34] was greater (by 6%, see Table 4) than that at 530.4 eV attributed to metal oxides [35]. Moreover, XPS technique proved to be useful to detect small quantities of carbonate phases (at 531.8 eV) on the surface of Fe(III)-150, which were not discovered by EXAFS and FTIR after having this phase volume averaged. It was confirmed by O 1s XPS that Fe (hydrous) oxides were the main Fe-containing phases in Fe(III)-150 as well on the surface, as demonstrated by XPS feature at 530.4 eV. The latter constituted 41.67% (O^{2-}, Fe oxides) compared with 9.06% of the

other species (assigned to {CO_3^{2-} + OH^-}). Very small quantities of water (revealed by band at 532.8 eV) appeared as a result of deconvolution of O 1s XPS spectra in Fe(III)-150 but not in Fe(II)-150. This outcome was in agreement with somewhat (hardly visible) greater amount of physiosorbed water in the former in contrast to the latter (the conclusion based on the FTIR examination, see Fig. 1), however both samples turned to be pretty dry materials.

C 1s XPS spectra, presented in Fig. 8, revealed the presence of two carbonate species (assigned to CO_3^{2-} and HCO_3^-) on the surface of Fe (II)-150 (peaks at 290.2 and 288.7 eV, respectively). However, only one carbonate form was measured in Fe(III)-150 (at 289.0 eV) shown by small single band, which was allocated to different species of CO_3^{2-} (compared with Fe(II)-150), most probably, hydrous carbonate, due to the presence of water (see Fig. 7). At that, at.% of iron carbonate species on the surface of Fe(II)-150 was almost 8 times greater than in the upper layer of Fe(III)-150, see Table 4.

3.6. Brief sorption tests of anion sorption on Fe(II)-150 and Fe(III)-150

Since the experiments reported in this paper were conducted within a pilot goal to develop new inorganic anion exchange adsorbents based on metal oxides, the samples (Fe(II)-150 and Fe(III)-150) were evaluated for their anion removal potential using seven aqueous anions: F^-, Br^-, BrO_3^-, $H_2AsO_4^-$, H_3AsO_3, $H_2PO_4^-$, SeO_4^{2-}. Results of the above studies are presented in Table 6.

Overall, none of the two composites, Fe(II)-150 and Fe(III)-150, exhibited a competitively strong sorption of any of the seven investigated anions, see Table 6. At the same time, anion removal of the former was stronger than of the latter. Sorption capability of Fe(II)-150 to arsenic species (arsenate and arsenite) was found to be on an approximately the same level as of the first commercial inorganic anion exchanger, developed in the beginning of 21st century, activated alumina (Al_2O_3) (<10 mg/g), [36]. Because composite Fe(III)-150 was grounded on Fe oxides, which were complemented by negligible quantities of Fe carbonate on the material surface, it was expected to be a stronger anion remover than Fe(II)-150, which was predominantly formed upon Fe carbonates, however the removal of the former of the several investigated anions was very weak. Fe(III)-150 did not sorb F^-

Table 6

Adsorptive capabilities of composites Fe(II)-150 and Fe(III)-150 to several anions. Experimental conditions: initial anion concentration = ~200 mg/L; adsorbent dose = 2 g/L; pH = 6.5 ± 2.

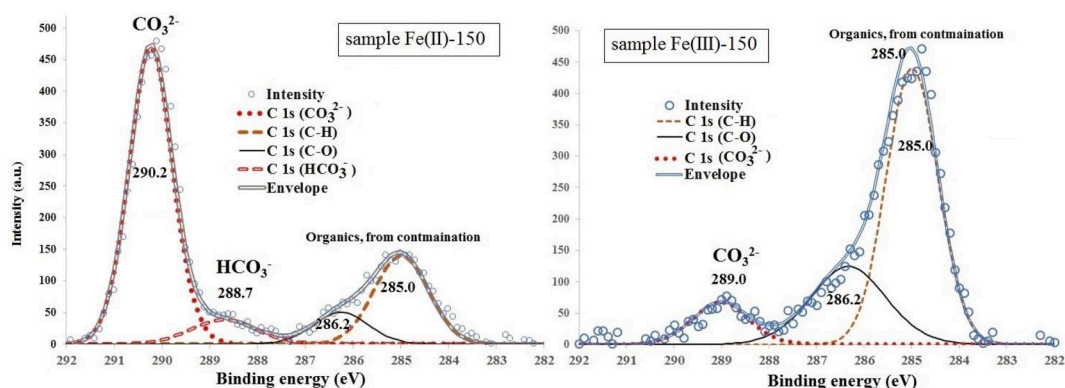| Sorbent	Adsorption, mg/g						
	F^-	Br^-	BrO_3^-	$H_2AsO_4^-$	As(III)	$H_2PO_4^-$	SeO_4^{2-}
Fe(II)-150	1.9	0.4	9.3	7.3	14.4	3.8	0
Fe(III)-150	0	2.5	3.4	3.6	4.3	1.7	0

Fig. 8. C 1s XPS spectra in samples Fe(II)-150 (left) and Fe(III)-150 (right).

and SeO_4^{2-} at all.

4. Discussion

4.1. Materials chemistry of Fe(II)-150 and Fe(III)-150 formed from divalent/trivalent Fe precursor, respectively

An idea to ground the preparation strategy of metal oxide-based material on using urea as hydrolyzer was caused by its well-known decomposition, which enriches the reacting media with OH^- groups (from ammonia) as well as with CO_2 according to (2):

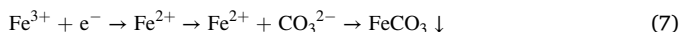$$(NH_2)_2CO + 3H_2O \rightarrow 2NH_4 \cdot OH + CO_2 \qquad (2)$$

OH^- and CO_2 entered a water solution can be utilized in a number of the material-precipitation reactions taking place in autoclave. When the initial mixture of reagents contained Fe^{2+} precursor, the materials chemistry was realized via the reactions (3) and (4):

$$Fe^{2+} + CO_3^{2-} \rightarrow FeCO_3 \downarrow \qquad (3)$$

$$Fe^{2+} + 2OH^- \rightarrow Fe(OH)_2 \downarrow \qquad (4)$$
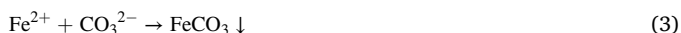
We cannot exclude that some oxidative precipitation of Fe(III) oxides from Fe(II) precursor could take place in autoclave, however reducing conditions (high pressure at a particular, fixed, high temperature, here, 150 °C) promoted the preferable generation of Fe(II)-based compounds. It is anticipated that oxidation of Fe^{2+} mainly developed outside of the autoclave, at the stages of filtration, washing and drying, see (5):

$$2Fe(OH)_2 + \frac{1}{2} O_2 + H_2O \rightarrow 2Fe(OH)_3 \downarrow \qquad (5)$$
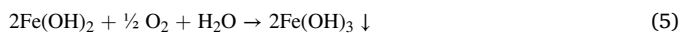
In case of utilization of Fe^{3+} precursor (instead of Fe^{2+}), it was directly involved in the precipitation of Fe(III) hydroxides according to (6) or, with fewer probability, in the reductive precipitation of Fe(II) carbonate (see (7)) due to high pressure in autoclave, which facilitated reduction of metal cations:

$$Fe^{3+} + 3OH^- \rightarrow Fe(OH)_3 \downarrow \qquad (6)$$

$$Fe^{3+} + e^- \rightarrow Fe^{2+} \rightarrow Fe^{2+} + CO_3^{2-} \rightarrow FeCO_3 \downarrow \qquad (7)$$

Solubility product constants of $Fe(OH)_2$, $Fe(OH)_3$ and $FeCO_3$ are equal to $2 \bullet 10^{-15}$; $6 \bullet 10^{-38}$; and $5 \bullet 10^{-11}$, respectively, [37]. We can always make theoretical predictions about dominating reactions in autoclave in both batches, using Fe(II)/Fe(III) precursors, however it is impossible to measure the intermediate products in a hermetically sealed autoclave. Thus, only experimental evidences obtained via characterization of the final solid products can provide a full (and real) explanation of the materials chemistry. Comparison of the entire precipitates (in bulk, volume averaged) with their surface chemistry (upper layer of 50 Å measurable by XPS) proved to be utmost important to interpret the materials chemistry of the above processes.

4.2. Differences of bulk chemical compositions in composites Fe(II)-150 and Fe(III)-150

At the superficial level (based on the solubility product constants [37]) we might have expected that hydrolysis of either Fe^{2+} or Fe^{3+} by access quantities of OH^- groups released from urea decomposition in autoclave would result in the formation of Fe hydrous oxides in both cases, regardless of the precursor oxidation state. However, the experimental evidences shown in this work proved that the chemical composition of the two samples differed dramatically from each other. In particularly, Fe(II)-150 was predominantly (>50%) formed by Fe carbonates while Fe(III)-150 was solely constructed upon Fe^{3+} oxides.

If we relied on the FTIR examination only we would have concluded that in sample Fe(II)-150, nearly >70% of Fe phases were the carbonate species, however, XANES Linear combination fitting gave us the precise ratio between Fe carbonates and Fe oxides, which constituted 56.2 and 43.8%, respectively. Nevertheless, results obtained by both techniques, FTIR and EXAFS, were in perfect agreement with each other, insisting on the fact that Fe(III) (hydrous) oxides were the only Fe substances in Fe (III)-150. Anyway, the latter sample was not a single crystal; it was founded upon several phases of Fe^{3+} (hydrous) oxides.

Moreover, examination of XANES pre-edge region allowed to reconfirm that Fe oxidation state in Fe(III)-150 was 100% Fe^{3+} but the ratio between Fe^{2+} and Fe^{3+} in Fe(II)-150 was found to be at 68/32%. Even if the XANES pre-edge review was highly useful tool, it seems to be less accurate than the LCF, see Fig. S2.

Simulation of Fe local structure in both composites reconfirmed the outcome of XANES LCF computation. It was demonstrated that although Fe(II)-150 was >50% based on Fe carbonate species, a great part of it was grounded on Fe oxide substances, which was reflected in both the first and the second shells of Fe. Complexity of this sample was mirrored already in the first shell: Fe–O distances in doublet (2.02 and 2.12 Å) corresponded to those in akageneite (second doublet peak at 2.04 Å) and siderite (2.15 Å), two different compounds. Second shell of Fe in Fe(II)-150 was fitted with C atoms using the main (the first, shorter and stronger) Fe–C path of siderite crystallography but the second Fe–C path of the latter was useless and unacceptable in simulation, which led us to the same conclusion: a great part, might be >40%, in Fe(II)-150 was different compound from Fe carbonate.

Similarity of the chemical nature of all phases in Fe(III)-150 was reconfirmed by EXAFS simulation of Fe local environment, very typical of Fe oxides, characterized by stronger second shell modeled solely using Fe–Fe paths. Fe–O interval in the first shell was equal to that in hematite, 1.95 Å, which fully correlated with the XRD patterns which revealed two crystalline phases: hematite and hydrohematite.

4.3. Dissimilarity of surface chemistry in Fe(II)-150 and Fe(III)-150 studied by XPS and discovery of residual, surface coverage, processes

Although XPS technique measures a narrow layer of sample surfaces of an approximately 30–50 Å, it is highly useful method to investigate interfacial phenomena (such as sorption and catalysis), to characterize new materials and interpret materials chemistry. For the later purpose it was helpful to compare the chemical compositions in the entire bulk sample (using XRD, EXAFS, FTIR etc.) and its upper layer (surface) studied by XPS. The chemical composition of each, Fe(II)-150 and Fe (III)-150, in bulk material (the entire sample, volume averaged) and on its surface differed from each other.

Throughout the sample Fe(II)-150 (volume averaged), majority of iron was found to be Fe^{2+}, due to the greater part of Fe(II) carbonates among the compounds formed this sample as proved by XANES (56.2%), EXAFS and FTIR. However, XPS demonstrated (Fig. 6) that on the surface, most iron occurred in oxidation state of Fe^{3+}. Such particularities of the sample structure arrangement can be explained by different leading reactions taking place in autoclave over time. While the autoclave was on at 150 °C, providing high temperature and pressure, the formation of Fe(II) carbonate dominated over Fe(III) oxides, which resulted in greater quantities of $FeCO_3$. After the autoclave was turned off and the pressure was dropped, Fe compound precipitation still took place for a while but the intensities of both processes changed. Generation of Fe oxides became a dominating reaction over formation of Fe carbonates, which resulted in the coverage of the previously formed particles (composed of $FeCO_3 + Fe(OH)_2$) mainly with species of Fe $(OH)_2$, which were further oxidized to $Fe(OH)_3$ on the stages of filtration, washing and drying. This conclusion was proved experimentally in Ref. [14], in which was demonstrated that percentage of Fe carbonates (compared with Fe hydrous oxides) proportionally increased as the autoclave temperature raised (120, 150 and 180 °C). Thus, when the temperature was dropped after the autoclave was turned off, precipitation of Fe oxides became a dominating process, see Ref. [14]. As a consequence, due to residual Fe oxide precipitation in the upper layer of

the composite particles, concentration of the surface carbonate (two species, CO_3^{2-} and HCO_3^-) measured by XPS constituted only 10.44% (Table 4), which is much less than the expected portion of $FeCO_3$ (56.2%) in the sample bulk, detected by XANES and confirmed by FTIR.

Based on the data obtained by XANES/EXAFS/FTIR, Fe^{2+} and $FeCO_3$ were not expected to be incorporated in sample Fe(III)-150, which indeed in bulk was fully composed of Fe(III) oxides. However, the upper thin layer of the sample particles contained divalent Fe (see Fig. 6) reflected by small quantities of carbon (1.35%) as carbonate species. If the respective amount of Fe carbonate was a representation of the volume averaged composition (in bulk), it would have been detectable by both XANES and FTIR, however the latter techniques did not measure any $FeCO_3$. This indicates that generation of some iron carbonate took place on the surface after the end of the main reactions, which formed the Fe-oxide-based carcass, the basis of this composite in bulk. We think that there were several preconditions, which made possible a reductive Fe^{3+} precipitation as $Fe^{2+}CO_3$ compounds. High concentration of CO_2 was accumulated in autoclave (unspent on any reaction) which created high pressure (kept for longer time after it was turned off) and consequently supported some reductive precipitation. Another reason might be the lowering of pH; it is known that precipitation of Fe carbonates can take place at the lower pH values than of Fe oxides. The preconditions above facilitated some residual formation of $FeCO_3$ on the surface in the reactive media with Fe(III) precursor which was an unpredictable process.

4.4. Confirmation of the recent hypotheses about using EXAFS-simulated metal (here, Fe) local structure in outer shell to explain anion exchange properties (via OH⁻) of metal oxides and hydration of physisorbed water

In [2,3] we pioneered exploring the outer shells of metals in metal oxides to explain their properties, additionally to traditional simulation of the 1st-2nd shells to refine the structure of new materials. In particularly, it was noted that outstanding adsorptive properties to aqueous anions were demonstrated by those Fe–Ce oxide/carbonate-based composites whose Fe outer shells were simulated by two paths ({Fe–Fe}+{Fe–O}) simultaneously applied to fit a single peak. It was suggested that one EXAFS band fitted with two atoms (Fe and O) in outer shells reflects an existence (location) of anion exchange sites abundant with OH⁻: O-(H) groups are attached to Fe-oxide phase. It was how we found a correlation between the adsorptive anion removal of ten Fe/Ce-based composites and their structure. In order to justify the behavior of ten metal(Fe/Ce)-oxide/carbonate based samples at the interface with water phase we had to go deeper, to the atomic scale using EXAFS, since traditional characterization techniques (XRD, specific surface area by N_2 adsorption, FTIR, XPS) did not establish an agreement between the material structure and its anion exchange properties.

The idea above was verified and extended in Ref. [14] in which we also continued exploring the EXAFS simulated outer shells of metals (here, Fe) in their oxide-based composites. In particularly, we made an additional observation that in the highly hydrated with physisorbed water Fe-oxide/carbonate-based composites (detected by FTIR), the outer shells of Fe were fitted with several oxygen (O) atoms (Fe–O paths). The reverse rule was also confirmed: in the driest sample, oxygen atoms were not applicable (no needed/useless) to simulate Fe outer shell, which were fitted with Fe–Fe paths only.

In this work, we confirmed both hypotheses presented in Refs. [2,3, 14]. It has been found that none of (single) EXAFS feature in Fe outer shell in any, Fe(II)-150 or Fe(III)-150, was fitted with two paths ({Fe–Fe}+{Fe–O}) simultaneously. This outcome correlates with the low anion removal performance of both composites. At the same time, none of the outer shell regions in any of these materials was modeled with several oxygen atoms (Fe–O paths), which additionally verified the conclusions made by FTIR about tiny amounts of physisorbed water in both samples shown by very small peaks at 1629 cm⁻¹.

4.5. Concluding remarks about the materials chemistry and the structure of Fe(II)-150 and Fe(III)-150

The temperature of 150 °C created high enough pressure in autoclave to provide an active precipitation not only $Fe(OH)_2$, but also $FeCO_3$ from Fe(II) precursor ($FeSO_4$). Moreover, the materials chemistry of Fe(II)-150 was even dominated by the formation of iron(II) carbonates. High pressure preserved Fe divalent oxidation state in the final (bulk, volume averaged) product as $FeCO_3$ at 56.2% measured by XANES LCF and approximately at 68% estimated by XANES pre-edge region of the spectra. However, after the end of the main reactions (autoclave was turned off) resulted in domination of Fe carbonate in the material bulk composition (over Fe(III) oxides), the surface of the particles was predominantly covered by Fe trivalent compounds (as Fe(III) hydrous oxides) detected by XPS surface analysis. As a result, the product particles were not homogeneous but were composed of the mostly iron carbonates in the center (in "nuclear") with increasing portion of Fe oxides on the surface. Such structure of the particles will be favorable in amendment of the composite composition via thermal or hydrothermal treatments because carbonate will facilitate further transformations of phases.

Materials chemistry of bulk Fe(III)-150 produced from Fe(III) precursor was more predictable. As expected, bulk sample (detectable by XANES/EXAFS/FTIR) was fully composed of Fe(III) hydrous oxides (100%), which were highly crystalline and constituted two phases: hematite (α-Fe_2O_3) and hydrohematite ($Fe1.833(OH)0.5O2.5$) (based on XRD patterns). However, the surface of the composite particles was slightly covered with Fe(II) carbonate (measured by both Fe 2p XPS and C 1s XPS), which was not dispersed over the entire material volume. Such unpredictable residual precipitation of $FeCO_3$ from precursor $Fe_2(SO_4)_3$ was caused by an access concentration of CO_2 released due to urea decomposition as well as the high pressure promoted reduction of Fe^{3+} cations. In our opinion, this composite shall not be recommended for preparation of different phases via further transformations during thermal or hydrothermal treatments. It is greatly composed of two stable phases, hematite and hydrohematite. However, thermal treatment of this composite will most probably result in pure phase of hematite (α-Fe_2O_3) due to transformation of hydrohematite into hematite.

Regardless of the choice of Fe(II)/Fe(III) precursor, both composites (Fe(II)-150 and Fe(III)-150) were pretty dry material, which indicates that the chosen temperature of 150 °C does not provide a high hydration property to materials. In contrast, at the temperatures of 120 and especially of 180 °C, the composites based on Fe oxides/carbonates were much hydrated samples than that formed at 150 °C, see Ref. [14]. Replacement of Fe precursor (Fe^{3+} instead of Fe^{2+}) did not change this property of 150°C-samples, which was one of the reasons why both composites (Fe(II)-150 and Fe(III)-150) demonstrated a low removal of toxic aqueous anions.

Since hydration is a very much wanted property of anion exchangers based on metal oxides (which act via exchange of their surface OH⁻ with aqueous anions), such experimental conditions (the temperature of 150 °C) shall not be recommended for synthesis of future anion exchange materials but might be useful for other applications in which hydration might be undesirable property.

5. Conclusions

Oxidation state of Fe precursor (Fe^{2+} or Fe^{3+}) strongly influenced both the materials chemistry in autoclave fixed at 150 °C for 24 h as well as the composition of solid synthesis products.

The presence of Fe^{2+} precursor promoted preferable precipitation of iron carbonates over iron oxides. High pressure and reducing conditions in autoclave facilitated the reactions of Fe^{2+}, which resulted in the ratio of Fe carbonates/oxides of 56.2/43.8%. However, the upper thin layer of the material particles was prevailed by Fe(III) oxides, in contract to the volume-averaged ratio of Fe carbonates/oxides.

As expected, in the Fe^{3+} precursor-initiated system, the chemical composition of volume-averaged products was fully composed of Fe(III) hydrous oxides most of which were hematite (α-Fe_2O_3) and hydrohematite ($Fe_{1.833}(OH)_{0.5}O_{2.5}$). However, the surface of the particles was partially covered with $FeCO_3$, which was not detectable for EXAFS, XANES and FTIR but was measured by XPS.

At the autoclave temperature of 150 °C, the synthesis products were always very dry inorganic composites based on Fe oxides/carbonates, which was the unwanted property of the future anion exchangers.

In case of Fe^{3+} precursor ($Fe_2(SO_4)_3$), the sample was more homogeneous and more crystalline, which resulted in fewer phases. It also indicated that a limited (minimum) number of materials chemistry reactions were possible compared with the Fe^{2+}-precursor system. Adsorptive removal of several anions (F^-, Br^-, BrO_3^-, $H_2AsO_4^-$, H_3AsO_3, $H_2PO_4^-$, SeO_4^{2-}) on this composite was uncompetitive based on the literature data.

Making use of Fe^{2+} precursor ($FeSO_4$) guaranteed a variety of the materials chemistry processes in autoclave, which improved the desired property of Fe oxide/carbonate-based composites by providing more solid phases. However, domination of Fe carbonates in the sample composition (which are not anion exchangers by chemical nature) and very low hydration prevented this material from being a highly competitive anion remover. Anyway, sorption of seven tested anions by this sample was stronger than by Fe(III)-150 prepared from Fe(III)-precursor.

The low overall sorption of several aqueous anions by both experimental composites has been a confirmation of the recently suggested hypothesis about using EXAFS simulated metal (here, Fe) local structure in outer shells to predict (or to explain) anion removal potential of metal oxides. In none of the two samples (Fe(II)-150 and Fe (III)-150), the Fe outer shell was simulated by two atoms (Fe + O) one peak, which would be an indication of abundance of $\underline{OH^-}$ on the surface of $\underline{Fe}$-based material at the distance of the initiation of solid-liquid interfaces.

In neither of the two composites the outer shells of Fe were simulated with several oxygen atoms, which validated the other hypothesis (of the year 2020), which correlated hydration of metal oxides (and maybe of other materials) with EXAFS simulated extended fine structure in outer shells to be modeled with several (many) oxygen atoms (using Fe–O paths).

In general, Fe^{3+} precursor can be recommended for preparation of pure (Fe(III) oxide) phases of very low hydration for applications different from sorption. Utilization of Fe^{2+} precursor results in generation of a variety of composite phases among which dominates $FeCO_3$. Although this is not the respective chemical nature of anion exchangers, such (iron carbonate-abundant) samples can be used as precursors for further transformations of the composite composition via thermal or hydrothermal treatments to produce different (wanted) materials. The presence of carbonate will always facilitate such alterations of phase composition.

Contribution of each author of the manuscript

"Effect of Fe oxidation state ($+2$ versus $+3$) in precursor on the structure of Fe oxides/carbonates-based composites examined by XPS, FTIR and EXAFS" by Natalia Chubar, Vasyl Gerda, Małgorzata Szlachta, Ganna Yablokova. Dr. Natalia Chubar: Attracted funds, led the group of the researchers (supervised Dr. Vasyl Gerda and Dr. Malgorzata Szlachta), participated in recording EXAFS data, fully interpreted and simulated all EXAFS spectra, interpreted XPS and FTIR spectra, wrote this manuscript. Dr. Vasyl Gerda: Synthesized both new inorganic composites based on Fe oxides/carbonates, run all adsorption tests, participated in consideration of all results and in the preparation of the manuscript, participated in collection of EXAFS spectra, recorded FTIR spectra. Dr. Malgorzata Szlachta: Collected EXAFS spectra, contributed to preparation of the manuscript, discussion of results and data visualization. Dr. Ganna Yablokova: Recorded XRD patterns and participated

in their interpretation, contributed to discussion of results and data visualization.

Declaration of competing interest

The authors declare no financial or any other conflicts of interests with anybody.

Appendix A. Supplementary data

Supplementary data to this article can be found online at https://doi.org/10.1016/j.solidstatesciences.2021.106752.

References

[1] Y. Zhu, X. Zhang, K. Koh, L. Kovarik, J.L. Fulton, K.M. Rosso, O.Y. Gutiérrez, Inverse iron oxide/metal catalysts from galvanic replacement, Nat. Commun. 11 (2020) 3269, https://doi.org/10.1038/s41467-020-16830-4.

[2] N. Chubar, V. Gerda, D. Banerjee, G. Yablokova, Effect of Fe(II)/Ce(III) Dosage ratio on the structure and anion adsorptive removal of hydrothermally precipitated composites: insights from EXAFS/XANES, XRD and FTIR, J. Colloid Interface Sci. 487 (2017) 388–400, https://doi.org/10.1016/j.jcis.2016.10.060.

[3] N. Chubar, V. Gerda, D. Banerjee, Influence of 300°C Thermal conversion of Fe-Ce hydrous oxides prepared by hydrothermal precipitation on the adsorptive performance of five anions: insights from EXAFS/XANES, XRD and FTIR (companion paper), J. Colloid Interface Sci. 491 (2017) 111–122, https://doi.org/10.1016/j.jcis.2016.12.008.

[4] X.-Y. Xue, C.-H. Ma, C.-X. Cui, L.-L. Xing, High lithium storage performance of α-Fe_2O_3/graphene nanocomposites as lithium-ion battery anodes, Solid State Sci. 13 (2011) 1526–1530, https://doi.org/10.1016/j.solidstatesciences.2011.05.015.

[5] R. Mengmeng, M. Chuanxin, H. Yi, G. Jing, R. Yukui, T. Xinlian, Z. Qi, F. Xing, Z. Zetian, H. Tianqi, Z. Siyuan, Iron oxide nanoparticles as a potential iron fertilizer for peanut (Arachis hypogaea), Front. Plant Sci. 7 (2016) 815, https://doi.org/10.3389/fpls.2016.00815.

[6] F. Lv, L. Fu, E.P. Giannelis, G. Qi, Preparation of γ-Fe_2O_3/SiO_2-capsule composites capable of using as drug delivery and magnetic targeting system from hydrophobic iron acetylacetonate and hydrophilic SiO_2-capsule, Solid State Sci. 34 (2014) 49–55, https://doi.org/10.1016/j.solidstatesciences.2014.05.005.

[7] C. Manjunatha, N. Srinivasa, S. Samriddhic, C. Vidyac, S. Ashoka, Studies on anion-induced structural transformations of iron(III) (Hydr)oxide micro-nanostructures and their oxygen evolution reaction performance, Solid State Sci. 106 (2020) 106324, https://doi.org/10.1016/j.solidstatesciences.2020.106314.

[8] E.F. Bernstein, H.W. Sarkas, P. Boland, Iron oxides in novel skin care formulations attenuate blue light for enhanced protection against skin damage, J. Cosmet. Dermatol. 20 (2021) 532–537, https://doi.org/10.1111/jocd.13803.

[9] G. Baldauf-Sommerbauer, S. Lux, M. Siebenhofera, Sustainable iron production from mineral iron carbonate and hydrogen, Green Chem. 18 (2016) 6255–6265, https://doi.org/10.1039/C6GC02160C.

[10] Minerals are essential in pet food, health & nutrition, Oct. 29, https://www.petcurean.com/blog/minerals-are-essential-in-pet-food/, 2020 (Last assessed 15/07/2021).

[11] U. Schwertmann, R.M. Cornell, Iron Oxides in the Laboratory: Preparation and Characterization, 2nd, Completely Revised and Enlarged Edition, Wiley-VCH, 2020, p. 204.

[12] R.M. Cornell, U. Schwertmann, The Iron Oxides: Structure, Properties, Reactions, Occurrences and Uses, 2nd, Completely Revised and Extended Edition, Wiley-VCH, 2006, p. 703.

[13] J. Liang, L. Li, M. Luo, J. Fang, Y. Hu, Synthesis and properties of magnetite Fe_3O_4 via a simple hydrothermal route, Solid State Sci. 12 (2010) 1422–1425, https://doi.org/10.1016/j.solidstatesciences.2010.05.022.

[14] N. Chubar, V. Gerda, Atomic scale structure and surface chemistry of Fe oxide-based composites precipitated at various temperatures via urea-supported

hydrothermal synthesis, Solid State Sci. 106 (2020) 1–13, https://doi.org/10.1016/j.solidstatesciences.2020.106331.

[15] W. Yang, Z. Gao, J. Wang, B. Wang, L. Liu, Hydrothermal synthesis of reduced graphene sheets/Fe_2O_3 nanorods composites and their enhanced electrochemical performance for supercapacitors, Solid State Sci. 20 (2013) 46–53, https://doi.org/10.1016/j.solidstatesciences.2013.03.011.

[16] S.R. Mishra, H. Adhikari, D.L. Kunwar, C. Ranaweera, B. Sapkota, Facile hydrothermal synthesis of hollow Fe_3O_4 nanospheres: effect of hydrolyzing agents and electrolytes on electrocapacitive performance of advanced electrodes, Int. J. Metall. Met. Phys. 2 (7) (2017). ISSN: 2631-5076.

[17] J. Liu, I. Romer, S. Vi Yu Tang, E. Valsami-Jones, R.E. Palmer, Crystallinity depends on choice of iron salt precursor in the continuous hydrothermal synthesis of Fe–Co oxide nanoparticles, RSC Adv. 7 (2017) 37436–37440, https://doi.org/10.1039/c7ra06647c.

[18] L.M. Cursaru, R.M. Piticescu, D.V. Dragut, R. Morel, C. Thébault, M. Carrière, H. Joisten, B. Dieny, One-step soft chemical synthesis of magnetite nanoparticles under inert gas atmosphere. magnetic properties and in vitro study, Nanomaterials 10 (2020) 1500, https://doi.org/10.3390/nano10081500.

[19] F.N. Sayed, V. Polshettiwar, Facile and sustainable synthesis of shaped iron oxide nanoparticles: effect of iron precursor salts on the shapes of iron oxides, Sci. Rep. 5 (2015), 09733, https://doi.org/10.1038/srep09733.

[20] T. Okamoto, T. Nakamura, Y.O. Tahara, M. Miyata, K. Sakota, T. Yatsuhashi, Effects of ligand and solvent on the synthesis of iron oxide nanoparticles from Fe (acac)3 solution by femtosecond laser irradiation, Chem. Lett. 49 (2020) 75–78, https://doi.org/10.1246/cl.190751.

[21] N. Ajinkya, X. Yu, P. Kaithal, H. Luo, P. Somani, S. Ramakrishna, Magnetic iron oxide nanoparticle (IONP) synthesis to applications: present and future (review) 13 (2020) 4644, https://doi.org/10.3390/ma13204644.

[22] M. Szlachta, V. Gerda, N. Chubar, Adsorption of arsenite and selenite using an inorganic ion exchanger based on Fe-Mn hydrous oxide, J. Colloid Interface Sci. 365 (2012) 213–221, https://doi.org/10.1016/j.jcis.2011.09.023.

[23] S. Nikitenko, A. Beale, A. van der Eerden, S. Jacques, U. Leynaud, M. Óbrien, D. Detollenaere, R. Kaptein, B. Weckhuysen, W. Bras, Implementation of a combined SAXS/WAXS/QEXAFS set-up for time-resolved in situ experiments, J. Synchrotron Radiat. 15 (2008) 632–640, https://doi.org/10.1107/S0909049508023327.

[24] B. Ravel, M. Newville, *THENA, ARTEMIS, HEPHAESTUS*: data analysis for X-ray absorption spectroscopy using *IFEFFIT*, J. Synchrotron Radiat. 12 (2005) 537–541, https://doi.org/10.1107/S0909049505012719.

[25] Data base athttp://cars9.uchicago.edu/cgi-bin/atoms (PS: it was available online on this website when the data were treated in 2016).

[26] Y. Fei, D.J. Frost, H.K. Mao, C.T. Prewitt, D. Hausermann, In situ structure determination of the high-pressure phase of Fe_3O_4, Am. Mineral. 84 (1999) 203–206, https://doi.org/10.2138/am-1999-1-222.

[27] A.M. Jubb, H.C. Allen, Vibrational spectroscopic characterization of hematite, maghemite, and magnetite thin films produced by vapor deposition, Appl. Surf. Interfaces 2 (2012) 2804–2812, https://doi.org/10.1021/am1004943.

[28] https://xpssimplified.com/elements/iron.php last assessed 15/07/2021.

[29] Y. Kathiraser, J. Ashok, S. Kawi, Synthesis and evaluation of highly dispersed SBA-15 supported Ni-Fe bimetallic catalysts for steam reforming of biomass derived tar reaction, Catal. Sci. Technol. 4 (2006) 4327–4336, https://doi.org/10.1039/C5CY01910A.

[30] R.A. Crane, T.B. Scott, The effect of vacuum annealing of magnetite and zero-valent iron-nanoparticles on the removal of aqueous uranium, J. Nanotechnol. (2013) 11, https://doi.org/10.1155/2013/173625, article ID 173625.

[31] A.P. Grosvenor, B.A. Kobe, M.C. Biesinger, N.S. McIntyre, Investigation of multiplet splitting of Fe 2p XPS and boding of Fe compounds, Surf. Interface Anal. 36 (2004) 1464–1574, https://doi.org/10.1002/sia.1984.

[32] A. Matamoros-Veloza, R. Barker, S. Vargas, A. Neville, Iron calcium carbonate instability: structural modification of siderite corrosion films, ACS Appl. Mater. Interfaces 12 (2020) 49237–49244, https://doi.org/10.1021/acsami.0c14513.

[33] B. Xing, N. Graham, W. Yu, Transformation of siderite to goethite by humic acid in the natural environment, Commun. Chem. 3 (2020) 38, https://doi.org/10.1038/s42004-020-0284-3.

[34] https://xpssimplified.com/elements/oxygen.php. Last assessed 15/07/2021.

[35] http://www.xpsfitting.com/2012/01/common-o-1s-values.html. Last assessed 15/07/2021.

[36] P. Dhanasekaran, P.M. Satya Sai, C. Anand Babu, R. Krishna Prabhu, K.K. Rajan, Arsenic removal from groundwater by Anjili tree sawdust impregnated with ferric hydroxide and activated alumina, Water Supply 16 (2016) 115–127, https://doi.org/10.2166/ws.2015.119.

[37] www.wiredchemist.com. Last assessed 15/07/2021.